



HAL
open science

Observations of a Deep Submesoscale Cyclonic Vortex in the Arabian Sea

Charly de Marez, Xavier Carton, Stéphanie Corréard, Pierre L'Hégaret,
Mathieu Morvan

► **To cite this version:**

Charly de Marez, Xavier Carton, Stéphanie Corréard, Pierre L'Hégaret, Mathieu Morvan. Observations of a Deep Submesoscale Cyclonic Vortex in the Arabian Sea. *Geophysical Research Letters*, 2020, 47, 10.1029/2020GL087881 . insu-03683237

HAL Id: insu-03683237

<https://insu.hal.science/insu-03683237>

Submitted on 1 Jun 2022

HAL is a multi-disciplinary open access archive for the deposit and dissemination of scientific research documents, whether they are published or not. The documents may come from teaching and research institutions in France or abroad, or from public or private research centers.

L'archive ouverte pluridisciplinaire **HAL**, est destinée au dépôt et à la diffusion de documents scientifiques de niveau recherche, publiés ou non, émanant des établissements d'enseignement et de recherche français ou étrangers, des laboratoires publics ou privés.

Copyright

Geophysical Research Letters

RESEARCH LETTER

10.1029/2020GL087881

Key Points:

- A deep submesoscale cyclone was observed in the Arabian Sea
- The cyclone contained Red Sea Water on its rim
- This cyclone was generated at the mouth of Gulf of Aden, as a local current interacted with the bottom topography

Correspondence to:

C. de Marez,
 charly.demarez@univ-brest.fr

Citation:


de Marez, C., Carton, X., Corréard, S., L'Hégaret, P., & Morvan, M. (2020). Observations of a deep submesoscale cyclonic vortex in the Arabian Sea. *Geophysical Research Letters*, *47*, e2020GL087881. <https://doi.org/10.1029/2020GL087881>

Received 9 MAR 2020

Accepted 20 MAY 2020

Accepted article online 30 MAY 2020

Observations of a Deep Submesoscale Cyclonic Vortex in the Arabian Sea

Charly de Marez¹ , Xavier Carton¹, Stéphanie Corréard², Pierre L'Hégaret¹, and Mathieu Morvan¹

¹Univ. Brest, Laboratoire d'Océanographie Physique et Spatiale (LOPS), IUEM, Plouzané, France,

²SHOM/DOPS/STM/DTO, Toulouse, France

Abstract Submesoscale coherent vortices (SCVs) are numerous in high-resolution numerical simulations, but their observations are scarce. Among the few in situ available measurements of SCVs, a vast majority concern anticyclones. No cyclonic SCV with large dynamical Rossby number ($|\zeta/f| > 1$) has ever been sampled. This suggested that such small cyclones may lack robustness. Here, we present in situ measurements of an intense cyclonic SCV in the Arabian Sea. This eddy lay at 600 m depth, with a Rossby number $Ro = \mathcal{O}(1)$ and a dynamical Rossby number $|\zeta/f| > 1.5$. This cyclone was most likely generated at the mouth of the Gulf of Aden. It trapped and advected Red Sea Water, from there on. This highlights the role of deep SCVs in the spreading of salty waters across the Arabian Sea.

Plain Language Summary Numerical simulations of the ocean reveal the presence of numerous submesoscale eddies, vortices with radii smaller than, or equal to, 10 km. Nevertheless, their observations at depth are scarce because sampling their hydrological and dynamical structures requires very high resolution measurements. The present study presents measurements of a deep submesoscale cyclone in the Arabian Sea, collected during the PHYSINDIEN 2019 experiment. This intense, submesoscale, subsurface cyclone was centered at 600 m depth; most likely, it was formed at the mouth of the Gulf of Aden. Then it carried highly saline waters from the Red Sea toward the open Arabian Sea. We underline that conditions leading to the formation of such submesoscale eddies are often met in this region. Thus, such deep eddies should be recurrent in this region and should play a key role in spreading salty waters.

1. Introduction

Mesoscale eddies (with radii ~ 100 km) are known as oceanic coherent structures. The increase in remote sensing capabilities (Chelton et al., 2007, 2011) helped improve the deployment of in situ sensors in the core of surface eddies. Altimetry and infrared radiometry allowed the tracking of such eddies in near real time and provided their characteristics at the ocean surface. Both surface- and subsurface-intensified eddies have a significant impact on biological activities, tracer transport, and properties of the water column (Chelton et al., 2011; Dong & McWilliams, 2007; Zhang et al., 2014).

At scales below the mesoscale, in particular at submesoscale (0.3–30 km horizontally), numerous physical phenomena, and in particular smaller coherent structures, play an important role in the evolution of the ocean. Submesoscale oceanic structures can be generated by the interaction of regional currents with the topography, or by the interaction of mesoscale structures, or by the instability of mesoscale currents. External forcings—for example, outflows, extreme wind events, and thermal vents—can also yield submesoscale structures (D'Asaro, 1988; de Marez et al., 2020; McWilliams, 2019). These submesoscale features, among which vortices and filaments (with a typical size on the order of 10 km), are more arduous to detect than mesoscale eddies, all the more so as they lie below the ocean surface.

Surface-intensified submesoscale features can be located via satellite measurements. With this information, sensors can be accurately deployed to measure the vertical structure of these small vortices and filaments (Buckingham et al., 2017; Chavanne & Klein, 2010; Lévy et al., 2012). Surface submesoscale features play a key role in the ocean primary production (Lévy et al., 2018) and in the restratification of surface layers (Boccaletti et al., 2007).

By contrast, the quantification and dynamics of subsurface-intensified submesoscale structures are much less known because measurements are scarce, all the more so for deep (>300 m depth) structures, whose presence cannot be detected by satellites. Their in situ sampling thus relies on either an accurate knowledge of deep dynamical processes (sampling locations must be chosen based on what we know about submesoscale structure formation) or luck (a sampling not specifically targeting the submesoscale but with sufficient resolution to encounter them).

Submesoscale coherent vortices (SCVs; McWilliams, 1985), also named intrathermocline eddies (ITEs; Dugan et al., 1982), are a type of such subsurface submesoscale structures. Their radii are smaller than the Rossby deformation radius, their velocity maxima are localized at depth (McWilliams, 1985), and they have high values of vorticity ζ , locally reaching the Coriolis frequency f , that is, $|\zeta/f| = \mathcal{O}(1)$ (McWilliams, 2019). A few in situ experiments succeeded in measuring SCVs with a sufficient horizontal resolution (see, e.g., Bosse et al., 2016, 2017; Gula et al., 2019; Kostianoy & Belkin, 1989; L'Hégaret et al., 2016; Lukas & Santiago-Mandujano, 2001; Meunier et al., 2018, and the references therein). Among these, only a few observations of *cyclonic* SCVs were reported (Bosse et al., 2016), but with weak horizontal velocities, and therefore $|\zeta/f| \ll 1$. Thus, in observations, intense SCVs appeared as strictly anticyclonic. This view was also supported by numerical and theoretical studies, which claim that isolated cyclonic vortices are more unstable than anticyclonic ones, with growth rates of most unstable perturbation being larger for cyclones than for anticyclones (Lazar, Stegner, & Heifetz, 2013; Lazar, Stegner, Caldeira, et al., 2013; Mahdinia et al., 2017; Stegner & Dritschel, 2000). However, it is currently not possible to definitely conclude on SCV stability properties with respect to their polarity, because of the lack of cyclonic SCV observations. Furthermore, most of SCV observations were impaired by a lack of direct velocity measurements preventing an accurate estimate of SCVs' dynamical structure.

SCVs can be generated by the interaction of boundary currents with topography (D'Asaro, 1988), by winter-time deep convection (Bosse et al., 2016), or by the natural or forced instability of deep flows (L'Hégaret et al., 2016). They are generated in numerous places, and they should be rather ubiquitous in the world oceans. In particular, SCVs can play a key role in salt transport. As examples, Lukas and Santiago-Mandujano (2001) measured an SCV that transported salty water from the coast of Baja California to Hawaii, thus increasing the local salinity by >0.5 psu. L'Hégaret et al. (2016) showed that, occasionally, SCVs formed at the mouth of the Persian Gulf can induce salinity anomalies up to 1 psu in the open Arabian Sea.

Due to strong evaporation, salty waters are formed in the marginal seas of the Arabian Sea; they are called the Persian Gulf Water (PGW) and the Red Sea Water (RSW). After flowing via the Strait of Hormuz or the Strait of Bab el Mandeb into the Arabian Sea, they settle at 300 and 600 m depths, respectively (Bower et al., 2000). In the Arabian Sea, the pathways and spreading of PGW and RSW are controlled by the deep dynamical influence of surface mesoscale eddies (Bower & Furey, 2012; L'Hégaret et al., 2015, 2016). SCVs have also been shown to carry PGW (L'Hégaret et al., 2016) and RSW (Meschanov & Shapiro, 1998; Shapiro & Meschanov, 1991) far from the straits. This suggests that deep submesoscale processes are important for the spreading of salty outflows in the Arabian Sea.

In this paper, we present an observation of an intense deep submesoscale cyclone in the Arabian Sea. It is intensified at the depth of the RSW, with this water mass characteristic; thus, it participates in the spreading of RSW in the Arabian Sea. In Section 2, we present the PHYSINDIEN experiment and the other data sets used in the study. In Section 3, we present in details the measured deep submesoscale cyclone. In Section 4, we discuss the possible generation mechanism of this cyclone. Finally, we summarize observations and conclude on the potential impact of these measurements in Section 5.

2. Data and Methods

2.1. The PHYSINDIEN 2019 Experiment

During the PHYSINDIEN 2019 experiment in May 2019, the French Navy oceanographic vessel BHO Beautemps-Beaupré measured the surface and subsurface circulation off the Omani coast (western Arabian Sea). The first part of the experiment (Leg 1) started from Salalah (Oman) on 2 May 2019 and reached Muscat (Oman) on 12 May 2019. During Leg 1, several devices were deployed including a vessel-mounted acoustic Doppler current profiler with 38 kHz frequency (RDI 38 kHz VM-ADCP) and a RapidCAST (off-the-shelf Teledyne product).

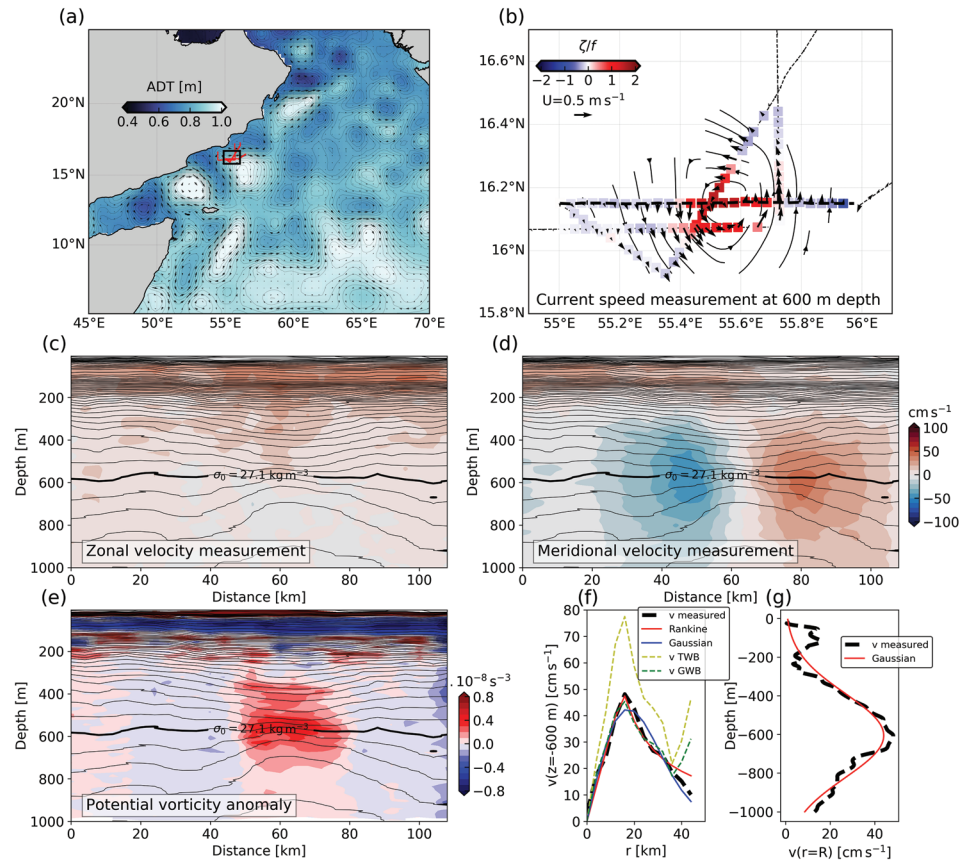


Figure 1. Dynamical structure of the deep submesoscale cyclone sampled off Omani coast. (a) Sea-level anomaly from AVISO and derived geostrophic surface current (black arrows) on 5 May 2019; the red lines indicate the ship track, and the black rectangle shows the position of panel (b). (b) Current speed measurement at 600 m depth from VM-ADCP measurements (black arrows) and normalized vorticity ζ/f along the ship track (colored squares) estimated from a linear optimal interpolation of horizontal velocities at 600 m depth (black streamlines); the thin dashed lines indicate the ship track, and the bold dashed line indicates the position of the vertical section shown in panels (c)–(e). (c) Vertical section of zonal velocity from VM-ADCP measurements along the east-west section shown bold in (b); thin black contours show isopycnals with a spacing of 0.1 kg m^{-3} , and thick black contour shows the $\sigma_0 = 27.1 \text{ kg m}^{-3}$ isopycnal. (d) Same as (c) for the meridional velocity along the east-west section shown bold in (b). (e) Same as (c) for the potential vorticity anomaly PVa along the east-west section shown bold in (b). (f) Profile of azimuthal velocity of the cyclone at 600 m depth from VM-ADCP measurements (dashed black), compared with estimates of the velocity using the thermal wind balance (TWB, dashed yellow) and the gradient wind balance (GWB, dashed green); fit of a Rankine vortex profile (solid red), with $R = 15.2 \pm 0.3 \text{ km}$, $V_0 = 0.50 \pm 0.01 \text{ m s}^{-1}$, and $\chi = 0.0328 \text{ m s}^{-1}$; fit of a Gaussian vortex profile (solid blue), with $R = 12.4 \pm 0.2 \text{ km}$, $V_0 = 0.49 \pm 0.01 \text{ m s}^{-1}$, and $\chi = 0.0345 \text{ m s}^{-1}$. (g) Vertical profile of velocity at the radius of maximum velocity ($r = 16 \text{ km}$) from ADCP measurements; fit of a vertical Gaussian profile, with $z_0 = -605 \pm 2 \text{ m}$, $H = 309 \pm 3 \text{ m}$, $V_0 = 0.44 \pm 0.01 \text{ m s}^{-1}$, and $\chi = 0.046 \text{ m s}^{-1}$.

During the whole Leg 1, the VM-ADCP measured the current velocity from ~ 40 to about 1,000 m depth. The vertical averaging of raw data is made over 16 m. On the horizontal, data are averaged every 200 m, with a ship speed of $\sim 4 \text{ m s}^{-1}$. This leads to an accuracy of velocity measurements of about $1.5 \times 10^{-2} \text{ m s}^{-1}$ (Jimenez-Gonzalez et al., 2003). The data were first linearly interpolated on a regularly spaced grid, with a horizontal resolution of 0.25 km and a vertical resolution of 1 m. Then, a low-pass filter with a cutting length of 5 km was applied on the horizontal to remove spurious fine-scale signals.

The RapidCAST sampled the salinity and the temperature of the water column during one particular section of Leg 1 (see bold dashed line in Figure 1b). This device is an automated profiler that performs CTD casts down to $\sim 500 \text{ m}$ at 5 knots and to $\sim 1,000 \text{ m}$ at 1 knot, without the requirement of an operator on deck. Along the section, 30 profiles, down to $\sim 1,000 \text{ m}$ depth, were acquired, spaced of 2 nautical miles ($< 4 \text{ km}$). The vertical resolution is here $\sim 1 \text{ m}$; it depends on the speed of the ship. The data were linearly interpolated on a regularly spaced grid, with a horizontal resolution of 4 km and a vertical resolution of 5 m.

The potential density referenced at the surface σ_0 was computed along this section, from the absolute salinity S_A and conservative temperature Θ , using the TEOS-10 equation of state for seawater (McDougall & Barker, 2011). Along this section, the VM-ADCP measurements were interpolated on the RapidCAST grid, in order to estimate the potential vorticity (PV) anomaly associated with the measured structure. PV is calculated via (Hoskins, 1974)

$$Q = \left(f + \frac{\partial v}{\partial x} \right) \frac{\partial b}{\partial z} - \frac{\partial v}{\partial z} \frac{\partial b}{\partial x}, \quad (1)$$

where x is the zonal position, v the VM-ADCP measured meridional velocity, f the Coriolis frequency, and $b = -g\sigma_0/\sigma_0^*$ the buoyancy (g is the gravity and σ_0^* the mean value of density). The PV anomaly (PVa) is computed by subtracting a climatological value of PV from the local PV, on each isopycnal; climatological PV is defined as $Q_{\text{clim}} = f \frac{\partial}{\partial z} b_{\text{clim}}$ —where b_{clim} is estimated from the WOA 2018 database (see details below). We performed several sections initially to confirm that the RapidCAST section passes through the center of the vortex.

2.2. Other Data Sets and Methods

To estimate the climatological thermohaline properties of the water column in the area of interest, we used the WOA 2018 database, supplied by NOAA. Temperature and salinity are provided for each month of the year, over the whole Arabian Sea. Its horizontal resolution is 0.25° , and its vertical resolution in the upper 1,500 m of the ocean is about 3 m.

We also used the MERCATOR reanalysis, to describe the ocean dynamics at depth and to obtain the fine-scale variations of thermohaline properties in the area of interest. This product, processed by CMES, supplies physical fields on a $1/12^\circ$ grid and 50 vertical levels, for the period 27 December 2006 to present. The salinity and the horizontal velocity field were linearly interpolated on the $\sigma_0 = 27.1 \text{ kg m}^{-3}$ isopycnal—near which RSW propagates (Bower et al., 2000).

We ran a particle advection simulation, using the aforementioned MERCATOR reanalysis data interpolated on the $\sigma_0 = 27.1 \text{ kg m}^{-3}$ isopycnal, with the set of Python classes Parcels (Probably A Really Computationally Efficient Lagrangian Simulator). This software simulates the advection of an ensemble of particles, using a given 2-D or 3-D velocity field. This tool has been widely used in the past few years, and it is fully described in Lange and van Sebille (2017) and Delandmeter and van Sebille (2019) and in the references therein.

3. The Submesoscale Cyclonic Vortex

3.1. Dynamical Structure

At the edge of a surface-intensified mesoscale anticyclone (see Figure 1a), measurements of horizontal currents were performed during the PHYSINDIEN 2019 experiment between 3 and 5 May 2019; they showed a velocity signal intensified at 600 m depth, off the Omani coast. The ship made several passes over the signal in a time lapse of about 24 hr, thus ensuring a synoptic sampling of the structure. Based on these measurements, the structure can be identified as a deep cyclonic vortex (Figure 1b). Its horizontal extent was about half the local first baroclinic Rossby radius of deformation (which is about 60 km in this region; see Chelton et al., 1998): It is a submesoscale cyclone (SCY hereafter in the text).

From these measurements, we find that the core of the SCY has vorticity values $\zeta/f > 1.5$ (see Figure 1b). Along sections performed through the SCY's center, isopycnals have a concave lens shape, typical of subsurface-intensified cyclones (Assassi et al., 2016; see Figures 1c–1e). Also, the SCY's PVa is that of an isolated cyclonic lens, relatively well isolated from the surrounding flow (see Figure 1e). The PVa reaches a peak value of $\mathcal{O}(10^{-8}) \text{ s}^{-3}$, and it is centered around the $\sigma_0 = 27.1 \text{ kg m}^{-3}$ isopycnal. The radial distribution of azimuthal velocity at 600 m depth is shown in Figure 1f. In its core, the SCY has a radial profile of azimuthal velocity close to that of a Rankine vortex profile:

$$v_{\text{Rankine}}(r) = V_0 \left(\frac{r}{R} \right) \text{ for } r < R, \quad (2)$$

where $R = 15.2 \text{ km}$ is the radius of the maximal azimuthal velocity $V_0 = 0.5 \text{ m s}^{-1}$. This can also be seen in the horizontal distribution of ζ (Figure 1b); relative vorticity is positive and does not vary much in the SCY's core. At the SCY's edge, the velocity profile is closer to that of a Gaussian vortex:

$$v_{\text{Gaussian}}(r) = V_1 \left(\frac{r}{R_1} \right) e^{-r^2/(4R_1^2)}, \quad (3)$$

with $R_1 = 12.4$ km and $V_1 = 0.49$ m s⁻¹ than to that of a Rankine vortex

$$v_{\text{Rankine}}(r) = V_0 \left(\frac{R}{r} \right) \text{ for } r > R. \quad (4)$$

This is most likely due to the background flow (Amores et al., 2017), which generates an opposite-signed vorticity shield around the eddy (Figure 1b) and therefore a Gaussian-like velocity profile. Over the whole vortex, the cumulative error of the Rankine fit, estimated as

$$\chi = \sqrt{\frac{1}{\int dr} \int dr (v_{\text{measured}} - v_{\text{fit}})^2},$$

is smaller than the error of the Gaussian fit. This difference is not statistically significant, as the profiles are different only over a few points. However, the observed SCY can rather be well represented by a Rankine vortex profile. The dependency of the azimuthal velocity with depth z follows a Gaussian law

$$v(R, z) = V_0 e^{-(z-z_0)^2/H^2}, \quad (5)$$

with $z_0 = -605$ m and $H = 309$ m, the depth and thickness of the SCY, respectively (see Figure 1g). The Gaussian shape of SCVs commonly used in past studies since McWilliams (1985) is thus rather satisfying to represent the SCY on the vertical, even if the actual profile of velocity is little skewed relative to the analytical shape.

From these characteristics, we estimate that the Rossby number $Ro = V_0/fR$, associated with the SCY, is $\mathcal{O}(1)$. Along with the value of the dynamical Rossby number $|\zeta/f| \sim 1.5$ (which is the relevant parameter to quantify ageostrophic effects; see Stegner & Dritschel, 2000), this suggests that the vortex is not in geostrophic balance. This is confirmed by the comparison between an estimate of the SCY's velocity, from its density signature, using (1) the thermal wind balance or (2) the gradient wind balance (Figure 1f). The gradient wind balance velocity is closer to the measured velocity of the SCY. The centrifugal acceleration due to eddy curvature balances in part the radial pressure gradient. This acts to decrease the azimuthal velocity of the cyclone.

3.2. Thermohaline Structure

The temperature and salinity profiles (Figures 2a and 2b) reveal that the SCY is surrounded by salty (>36 g kg⁻¹) and warm ($>11^\circ\text{C}$) water, in comparison to climatological values (Figure 2e). This water mass has the thermohaline signature of RSW, and it is centered around the $\sigma_0 = 27.1$ kg m⁻³ isopycnal (Figure 2e) (Bower et al., 2000).

Layering is seen in the high salinity profiles that surround the SCY (Figure 2c), suggesting that double diffusive processes occur. This is confirmed by the values of Turner angle Tu (Ruddick, 1983; Turner, 1979), defined a

$$Tu = \tan^{-1} \left(\frac{\delta + 1}{\delta - 1} \right), \quad (6)$$

with $\delta = \frac{\beta \partial_z S_A}{\alpha \partial_z \Theta}$, where β and α are the thermal expansion coefficient and the saline contraction coefficient, respectively. Where $-90^\circ < Tu < -45^\circ$, the water column is diffusively unstable: Warm and salty waters are found below colder and fresher waters leading to stable diffusive convection; where $45^\circ < Tu < 90^\circ$, warm and salty waters are found above colder and fresher ones, leading to favorable conditions for salt fingering; and where $-45^\circ < Tu < 45^\circ$, the water column is stable with respect to double diffusion.

The upper core of the SCY (i.e., between 200 and 600 m depth) is stable. However, the lower core of the SCY (i.e., between 600 and 1,000 m depth), as well as its edge, exhibits values of Tu in the range $-90^\circ < Tu < -45^\circ$ (Figure 2d). The SCY is thus subject to double diffusive convection, which can in turn lead to a vertical homogenization of the water column properties. Such processes are supposed to induce a long-time decay of the SCY (McWilliams, 1985).

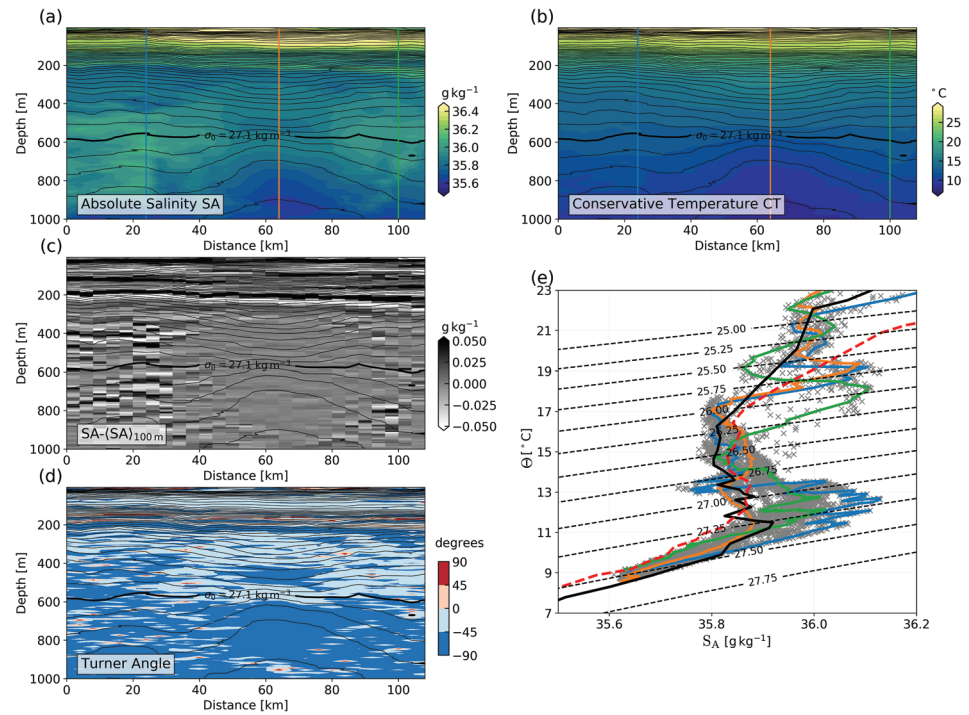


Figure 2. Thermohaline structure of the deep submesoscale cyclone. (a) Same as Figure 1c for the absolute salinity S_A from RapidCAST measurements. (b) Same as (a) for the conservative temperature Θ . (c) Same as (a) for the difference between the measured S_A and vertically low-passed S_A $\langle S_A \rangle_{100\text{m}}$ with a cutting length of 100 m. (d) Same as (a) for the Turner angle Tu . (e) Temperature-salinity diagram containing all profiles shown in panels (a) and (b); the blue and green (resp. orange) profiles show profiles collected at the edge (resp. center) of the cyclone (see their position in panels a and b), and the thick solid black (resp. dashed red) profile shows the TS profile (from the WOA 2018 database) at the proposed site of generation (resp. site of observation) shown in Figures 3a–3d by the red (resp. green) cross.

4. Discussion on the Origin of the Vortex

Unfortunately, the only available information about the SCY comes from measurements performed once at the observation site, as described in Section 3. Its past life is unknown. No Argo profiling float sampled it. During the 3 months prior to SCY discovery, the only data available at this location were satellite data. Since the SCY has no surface signature, satellite data do not provide information on its origin nor on its path.

However, a numerical model that assimilates satellite data such as MERCATOR can provide realistic surface fields with a satisfactory horizontal resolution, along with an estimate of thermohaline and dynamical properties of the ocean at depth. Thus, we assume here that the SCY evolved passively, on a given isopycnal, advected by the mean current from its generation site to its observation site (the green cross in Figures 3a–3c). This assumption is reasonable, since the SCY has a lens-like structure and a coherent core; past studies have shown that SCVs are robust; they can live for several months steadily or advected by large-scale or mesoscale flows (McWilliams, 1985).

Starting from this assumption, we release particles around the observation site and advect them backward during 3 months using the MERCATOR reanalysis velocities on the $\sigma_0 = 27.1 \text{ kg m}^{-3}$ isopycnal. Thus, we obtain an estimate of the previous path of water particles trapped inside the SCY. A large amount of particles (17%) comes from the easternmost part of the Gulf of Aden; they passed close to a prominent topographic feature, the Ra’s Fartak cape (see the red cross in Figures 3a–3c), on average on mid-March of 2019. Other particles remained in the open ocean, far away from the coast.

The SCY has plausibly been generated at the entrance of the Gulf of Aden, by interaction between the mean flow and the Ra’s Fartak cape. Other generation sites can be excluded for two reasons. First, the impermeability theorem (Haynes & McIntyre, 1990) states that no PV transport is possible across isopycnal surfaces, except if frictional or diapycnal processes occur. Thus, the high PVa values of the SCY on the $\sigma_0 = 27.1 \text{ kg m}^{-3}$ isopycnal must have been generated by deep nonconservative or diabatic effects

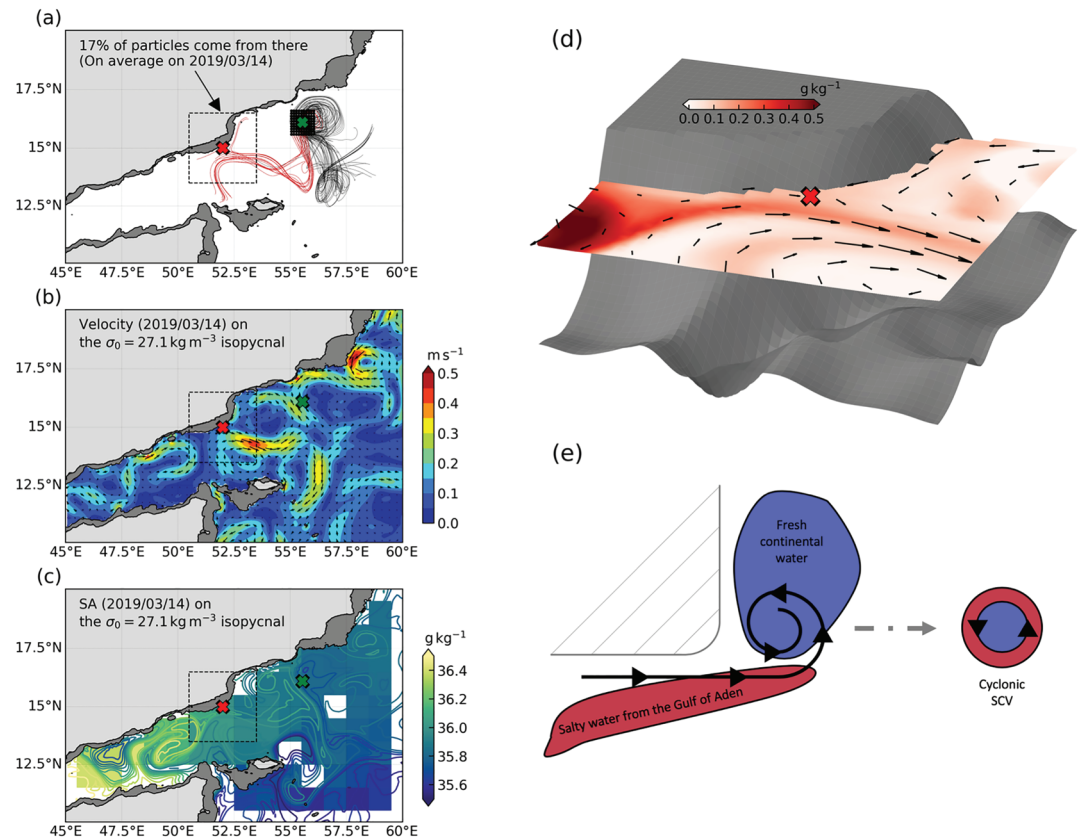


Figure 3. Proposed mechanism of generation of the deep submesoscale cyclone. (a) Trajectories of 100 particles initially placed at the observation site (green cross) and advected backward using the velocities of the MERCATOR reanalysis on the $\sigma_0 = 27.1 \text{ kg m}^{-3}$ isopycnal; red lines indicate the trajectories of particles that passed close to the proposed generation site, the Ra's Fartak cape (red cross), during their journey. (b) Horizontal velocity from the MERCATOR reanalysis on the $\sigma_0 = 27.1 \text{ kg m}^{-3}$ isopycnal, on the average date when advected particles passed close to the generation site (14 March 2019); the color shows the intensity of the current and arrows the direction. (c) Absolute salinity from the WOA 2018 database (color) and from the MERCATOR reanalysis (color contours), on the $\sigma_0 = 27.1 \text{ kg m}^{-3}$ isopycnal, on the same date than (b). (d) 3-D view of the generation site on 14 March 2019; the gray 3-D surface shows the bathymetry, the color plot shows the salinity anomaly (i.e., the difference from the WOA 2018 database), and the black arrows show the horizontal velocity, on the $\sigma_0 = 27.1 \text{ kg m}^{-3}$ isopycnal from the MERCATOR reanalysis. (e) Schematic of the proposed mechanism of generation of a deep cyclone by interaction with the topography, inspired from D'Asaro (1988).

(McWilliams, 1985). Following the particle trajectories, the only place where such a PV injection is possible is Ra's Fartak cape, via frictional effects at the bottom. Second, the thermohaline properties of the SCY's core are comparable with the climatological values at Ra's Fartak cape (see Figure 2e). If the SCY had been generated in the open Arabian Sea (following other particle trajectories), its core would have been fresher.

The proposed mechanism of generation is the following. Mid-March 2019, an anticyclonic mesoscale eddy at the mouth of the Gulf of Aden induced an intense current along Ra's Fartak cape, reaching 0.15 m s^{-1} at depth. As this current flowed eastward (see Figures 3b and 3d), with the coast on its left, frictional torques generated a positive vorticity strip close to the topography. This strip subsequently rolled up into small cyclones in the lee of the cape, possibly via inertia and the D'Asaro mechanism (D'Asaro, 1988) and/or by centrifugal and barotropic shear instabilities (Srinivasan et al., 2019). Frictional generation of vorticity near the coast has been intensively studied, using idealized (Dong et al., 2007; Morvan et al., 2019; Srinivasan et al., 2019) and realistic (Contreras et al., 2019; Dong & McWilliams, 2007; Gula et al., 2019, 2015; McWilliams, 2019; Vic et al., 2015) numerical simulations. It has been identified as an efficient mechanism to form deep submesoscale vortices in gradient wind balance, with high values of $|\zeta/f|$ (Srinivasan et al., 2019), and a lens-like shape (Morvan et al., 2019).

In particular, Srinivasan et al. (2019) showed that the value of $|\zeta/f|$ for a submesoscale vortex generated in the lee of a seamount scales as

$$|\zeta/f| \sim \frac{U}{fL} \mathcal{O}(h\sqrt{N}), \quad (7)$$

with N the ambient stratification and U the intensity of the current flowing over a seamount of height h and width L . We apply this scaling assuming that the Ra's Fartak cape induces the same dynamics than half of a seamount. We take $U = 0.15 \text{ m s}^{-1}$, $h = 1,500 \text{ m}$, $L = 50 \text{ km}$, $N = 2.5 \times 10^{-2} \text{ s}^{-1}$ (estimated with the WOA 2018 climatology), and $f = 3.77 \times 10^{-5} \text{ s}^{-1}$. This gives $1 < |\zeta/f| < 10$, which is in satisfactory agreement with the high values of $|\zeta/f|$ in the core of the observed SCY. Concomitantly with this vorticity generation, a tongue of salty water from the Gulf of Aden, with the signature of RSW, was advected along the coast (see Figures 3c and 3d) by the local current. This salty water wrapped around the newly formed SCY and, in turn, formed the ring of RSW observed around the SCY. The whole generation process is summarized in Figure 3e.

5. Conclusion

In this paper, we have presented an original observation of a deep SCY in the Arabian Sea. It was plausibly formed at the mouth of the Gulf of Aden, near Ra's Fartak cape, where the interaction of a mesoscale anticyclone with the steep topography provided a source of positive vorticity that subsequently generated a deep cyclone. During its formation, the cyclone entrained salty RSW (from the Gulf of Aden) along its rim. Then, it traveled for about 2 months, entering the Omani waters, where it was sampled. Temperature and salinity measurements show that the water surrounding the cyclone is saltier and warmer than the climatological value (see Figure 2e). The passage of the cyclone has thus—locally and transiently—contributed to increase the deep salinity and temperature of the Arabian Sea, by carrying RSW seaward. Moreover, if the cyclone has dissipated just after its observation, it could have had a lasting impact on salinity in that location.

Mesoscale anticyclones are regularly observed in the mouth of the Gulf of Aden, near Ra's Fartak cape (Morvan et al., 2020): the Summer Eddy, which is formed at the beginning of the summer monsoon and then travels into the Gulf of Aden (Bower & Furey, 2012); the Somali Current Rings, observed in October (Fratantoni et al., 2006); and the Gulf of Aden Eddy during the spring intermonsoon (Prasad et al., 2001). Therefore, the generation of deep SCYs may be a common phenomenon, though little observed for the moment due to their small size and to the absence of surface signature. Along Omani coasts, salinity peaks at the depth of RSW have been observed in the past (Carton et al., 2012; de Marez et al., 2019). They could be related to submesoscale structures carrying RSW away from their generation spot. Anticyclonic SCVs carrying salty RSW have already been observed in the Arabian Sea (Meschanov & Shapiro, 1998; Nof et al., 2002; Shapiro & Meschanov, 1991). They were most likely generated by the instability of the outflowing RSW tongue. Thus, several mechanisms that can lead to the generation of coherent SCVs are at play, in the Gulf of Aden. These results altogether suggest that deep submesoscale eddies may contribute substantially to the transport of RSW out of the Gulf of Aden and to the mean stratification at depth.

More generally, the observations presented in this paper show that, even if anticyclonic SCVs seem to be predominant in the deep ocean, cyclones can also be generated and remain coherent for several months. Here, the cyclone has a Rossby number $Ro = \mathcal{O}(1)$. This cyclone is thus very intense and highly ageostrophic. Its 3-D structure is close to theoretical profiles (close to that of a Rankine vortex radially and Gaussian vertically). The universality of such profiles should be studied with more real or simulated data. Further, we should study the mechanisms for polarity bias in SCVs, in particular intense ones, if such a bias is confirmed. For instance, stability studies could be conducted, using these simple analytical profiles, to further describe the processes at play in intense anticyclonic and cyclonic SCVs.

Data Availability Statement

The altimeter products were produced by SSALTO/DUACS and distributed by AVISO, with support from CNES. The WOA 2018 data set, the MERCATOR reanalysis, and the Parcels tool can be found online (<https://www.nodc.noaa.gov/OC5/woa18/woa18data.html>, <https://marine.copernicus.eu>, and <https://oceanparcels.org>). Processed data can be obtained on the author's GitHub (<https://github.com/demarez/DATA>; see de Marez, 2020).

Acknowledgments

This work was funded by the Direction Générale de l'Armement (DGA) via a full grant for Charly de Marez's PhD. The authors gratefully acknowledge helpful discussions with C. Vic, C. Buckingham, and T. Meunier. Finally, and most importantly, we address special thanks to the captain and crew of the oceanographic vessel BHO Beautemps-Beaupré, whose dedication allowed us to obtain the fine measurements presented here.

References

- Amores, A., Monserrat, S., Melnichenko, O., & Maximenko, N. (2017). On the shape of sea level anomaly signal on periphery of mesoscale ocean eddies. *Geophysical Research Letters*, *44*, 6926–6932. <https://doi.org/10.1002/2017GL073978>
- Assassi, C., Morel, Y., Vandermeersch, F., Chaigneau, A., Pegliasco, C., Morrow, R., & Cambra, R. (2016). An index to distinguish surface- and subsurface-intensified vortices from surface observations. *Journal of Physical Oceanography*, *46*(8), 2529–2552. <https://doi.org/10.1175/JPO-D-15-0122.1>
- Boccaletti, G., Ferrari, R., & Fox-Kemper, B. (2007). Mixed layer instabilities and restratification. *Journal of Physical Oceanography*, *37*(9), 2228–2250. <https://doi.org/10.1175/JPO3101.1>
- Bosse, A., Testor, P., Houpert, L., Damien, P., Prieur, L., Hayes, D., & Mortier, L. (2016). Scales and dynamics of Submesoscale Coherent Vortices formed by deep convection in the northwestern Mediterranean Sea: Vortices in the NW Mediterranean Sea. *Journal of Geophysical Research: Oceans*, *121*, 7716–7742. <https://doi.org/10.1002/2016JC012144>
- Bosse, A., Testor, P., Mayot, N., Prieur, L., D'Ortenzio, F., Mortier, L., & Raimbault, P. (2017). A submesoscale coherent vortex in the Ligurian Sea: From dynamical barriers to biological implications. *Journal of Geophysical Research: Oceans*, *122*, 6196–6217. <https://doi.org/10.1002/2016JC012634>
- Bower, A. S., & Furey, H. H. (2012). Mesoscale eddies in the Gulf of Aden and their impact on the spreading of Red Sea Outflow Water. *Progress in Oceanography*, *96*(1), 14–39. <https://doi.org/10.1016/j.pocean.2011.09.003>
- Bower, A. S., Hunt, H. D., & Price, J. F. (2000). Character and dynamics of the Red Sea and Persian Gulf outflows. *Journal of Geophysical Research*, *105*(C3), 6387–6414. <https://doi.org/10.1029/1999JC900297>
- Buckingham, C. E., Khaleel, Z., Lazar, A., Martin, A. P., Allen, J. T., Naveira Garabato, A. C., & Vic, C. (2017). Testing Munk's hypothesis for submesoscale eddy generation using observations in the North Atlantic. *Journal of Geophysical Research: Oceans*, *122*, 6725–6745. <https://doi.org/10.1002/2017JC012910>
- Carton, X., L'Hégaret, P., & Baraille, R. (2012). Mesoscale variability of water masses in the Arabian Sea as revealed by ARGO floats. *Ocean Science*, *8*(2), 227–248. <https://doi.org/10.5194/os-8-227-2012>
- Chavanne, C. P., & Klein, P. (2010). Can oceanic submesoscale processes be observed with satellite altimetry? *Geophysical Research Letters*, *37*, L22602. <https://doi.org/10.1029/2010GL045057>
- Chelton, D. B., deSzoeke, R. A., Schlax, M. G., El Naggar, K., & Siwertz, N. (1998). Geographical variability of the first baroclinic Rossby radius of deformation. *Journal of Physical Oceanography*, *28*(3), 433–460. [https://doi.org/10.1175/1520-0485\(1998\)028<0433:GVOTFB>2.0.CO;2](https://doi.org/10.1175/1520-0485(1998)028<0433:GVOTFB>2.0.CO;2)
- Chelton, D. B., Gaube, P., Schlax, M. G., Early, J. J., & Samelson, R. M. (2011). The influence of nonlinear mesoscale eddies on near-surface oceanic chlorophyll. *Science*, *334*(6054), 328–332. <https://doi.org/10.1126/science.1208897>
- Chelton, D. B., Schlax, M. G., & Samelson, R. M. (2011). Global observations of nonlinear mesoscale eddies. *Progress in Oceanography*, *91*(2), 167–216. <https://doi.org/10.1016/j.pocean.2011.01.002>
- Chelton, D. B., Schlax, M. G., Samelson, R. M., & de Szoeke, R. A. (2007). Global observations of large oceanic eddies. *Geophysical Research Letters*, *34*, L15606. <https://doi.org/10.1029/2007GL030812>
- Contreras, M., Pizarro, O., Dewitte, B., Sepulveda, H. H., & Renault, L. (2019). Subsurface mesoscale eddy generation in the ocean off central Chile. *Journal of Geophysical Research: Oceans*, *124*, 5700–5722. <https://doi.org/10.1029/2018JC014723>
- D'Asaro, E. A. (1988). Generation of submesoscale vortices: A new mechanism. *Journal of Geophysical Research*, *93*(C6), 6685. <https://doi.org/10.1029/JC093iC06p06685>
- de Marez, C. (2020). Submesoscale cyclone dataset. <http://github.com/demarez/DATA>. doi: 10.5281/zenodo.3824500.
- de Marez, C., L'Hégaret, P., Morvan, M., & Carton, X. (2019). On the 3D structure of eddies in the Arabian Sea. *Deep Sea Research Part I: Oceanographic Research Papers*, *150*, 103057. <https://doi.org/10.1016/j.dsr.2019.06.003>
- de Marez, C., Meunier, T., Morvan, M., L'Hégaret, P., & Carton, X. (2020). Study of the stability of a large realistic cyclonic eddy. *Ocean Modelling*, *146*, 101540. <https://doi.org/10.1016/j.ocemod.2019.101540>
- Delandmeter, P., & van Sebille, E. (2019). The Parcels v2.0 Lagrangian framework: New field interpolation schemes. *Geoscientific Model Development*, *12*(8), 3571–3584. <https://doi.org/10.5194/gmd-12-3571-2019>
- Dong, C., & McWilliams, J. C. (2007). A numerical study of island wakes in the Southern California Bight. *Continental Shelf Research*, *27*(9), 1233–1248. <https://doi.org/10.1016/j.csr.2007.01.016>
- Dong, C., McWilliams, J. C., & Shchepetkin, A. F. (2007). Island wakes in deep water. *Journal of Physical Oceanography*, *37*(4), 962–981. <https://doi.org/10.1175/JPO3047.1>
- Dugan, J. P., Mied, R. P., Mignerey, P. C., & Schuetz, A. F. (1982). Compact, intrathermocline eddies in the Sargasso Sea. *Journal of Geophysical Research*, *87*(C1), 385. <https://doi.org/10.1029/JC087iC01p00385>
- Fratantoni, D. M., Bower, A. S., Johns, W. E., & Peters, H. (2006). Somali Current rings in the eastern Gulf of Aden. *Journal of Geophysical Research*, *111*, C0903. <https://doi.org/10.1029/2005JC003338>
- Gula, J., Blacic, T. M., & Todd, R. E. (2019). Submesoscale coherent vortices in the Gulf Stream. *Geophysical Research Letters*, *46*, 2704–2714. <https://doi.org/10.1029/2019GL081919>
- Gula, J., Molemaker, M. J., & McWilliams, J. C. (2015). Topographic vorticity generation, submesoscale instability and vortex street formation in the Gulf Stream. *Geophysical Research Letters*, *42*, 4054–4062. <https://doi.org/10.1002/2015GL063731>
- Haynes, P. H., & McIntyre, M. E. (1990). On the conservation and impermeability theorems for potential vorticity. *Journal of the Atmospheric Sciences*, *47*(16), 2021–2031. [https://doi.org/10.1175/1520-0469\(1990\)047<2021:OTCAIT>2.0.CO;2](https://doi.org/10.1175/1520-0469(1990)047<2021:OTCAIT>2.0.CO;2)
- Hoskins, B. J. (1974). The role of potential vorticity in symmetric stability and instability. *Quarterly Journal of the Royal Meteorological Society*, *100*(425), 480–482. <https://doi.org/10.1002/qj.49710042520>
- Jimenez-Gonzalez, S., Mayerle, R., & Egozoue, J. (2003). On the accuracy of acoustic Doppler current profilers for in-situ measurements. A proposed approach and estimations for measurements in tidal channels. <https://doi.org/10.1109/CCM.2003.1194311>
- Kostianoy, A., & Belkin, I. (1989). A survey of observations on intrathermocline eddies in the world ocean. *Elsevier Oceanography Series* (Vol. 50, pp. 821–841). Moscow: Elsevier. [https://doi.org/10.1016/S0422-9894\(08\)70223-X](https://doi.org/10.1016/S0422-9894(08)70223-X)
- L'Hégaret, P., Carton, X., Louazel, S., & Boutin, G. (2016). Mesoscale eddies and submesoscale structures of Persian Gulf Water off the Omani coast in spring 2011. *Ocean Science*, *12*(3), 687–701. <https://doi.org/10.5194/os-12-687-2016>
- L'Hégaret, P., Duarte, R., Carton, X., Vic, C., Ciani, D., Baraille, R., & Corréard, S. (2015). Mesoscale variability in the Arabian Sea from HYCOM model results and observations: Impact on the Persian Gulf Water path. *Ocean Science*, *11*(5), 667–693. <https://doi.org/10.5194/os-11-667-2015>
- Lange, M., & van Sebille, E. (2017). Parcels v0.9: Prototyping a Lagrangian ocean analysis framework for the petascale age. *Geoscientific Model Development*, *10*(11), 4175–4186. <https://doi.org/10.5194/gmd-10-4175-2017>

- Lazar, A., Stegner, A., Caldeira, R., Dong, C., Didelle, H., & Viboud, S. (2013). Inertial instability of intense stratified anticyclones. Part 2. Laboratory experiments. *Journal of Fluid Mechanics*, 732, 485–509. <https://doi.org/10.1017/jfm.2013.413>
- Lazar, A., Stegner, A., & Heifetz, E. (2013). Inertial instability of intense stratified anticyclones. Part 1. Generalized stability criterion. *Journal of Fluid Mechanics*, 732, 457–484. <https://doi.org/10.1017/jfm.2013.412>
- Lévy, M., Ferrari, R., Franks, P. J. S., Martin, A. P., & Riviere, P. (2012). Bringing physics to life at the submesoscale. *Geophysical Research Letters*, 39, L14602. <https://doi.org/10.1029/2012GL052756>
- Lévy, M., Franks, P. J. S., & Smith, K. S. (2018). The role of submesoscale currents in structuring marine ecosystems. *Nature Communications*, 9(1), 4758. <https://doi.org/10.1038/s41467-018-07059-3>
- Lukas, R., & Santiago-Mandujano, F. (2001). Extreme water mass anomaly observed in the Hawaii ocean time-series. *Geophysical Research Letters*, 28(15), 2931–2934. <https://doi.org/10.1029/2001GL013099>
- Mahdinia, M., Hassanzadeh, P., Marcus, P. S., & Jiang, C. H. (2017). Stability of three-dimensional Gaussian vortices in an unbounded, rotating, vertically stratified, Boussinesq flow: Linear analysis. *Journal of Fluid Mechanics*, 824, 97–134. <https://doi.org/10.1017/jfm.2017.303>
- McDougall, T. J., & Barker, P. M. (2011). Getting started with TEOS-10 and the Gibbs Seawater (GSW) oceanographic toolbox. *SCOR/IAPSO WG, 127*, 1–28.
- McWilliams, J. C. (1985). Submesoscale, coherent vortices in the ocean. *Reviews of Geophysics*, 23(2), 165–182. <https://doi.org/10.1029/RG023i002p00165>
- McWilliams, J. C. (2019). A survey of submesoscale currents. *Geoscience Letters*, 6(1). <https://doi.org/10.1186/s40562-019-0133-3>
- Meschanov, S., & Shapiro, G. (1998). A young lens of Red Sea Water in the Arabian Sea. *Deep Sea Research Part I: Oceanographic Research Papers*, 45(1), 1–13. [https://doi.org/10.1016/S0967-0637\(97\)00018-6](https://doi.org/10.1016/S0967-0637(97)00018-6)
- Meunier, T., Tenreiro, M., Palls-Sanz, E., Ochoa, J., Ruiz-Angulo, A., Portela, E., & Carton, X. (2018). Intrathermocline eddies embedded within an anticyclonic vortex ring. *Geophysical Research Letters*, 45, 7624–7633. <https://doi.org/10.1029/2018GL077527>
- Morvan, M., L'Hégaret, P., Carton, X., Gula, J., Vic, C., de Marez, C., & Koshel, K. (2019). The life cycle of submesoscale eddies generated by topographic interactions. *Ocean Science*, 15(6), 1531–1543. <https://doi.org/10.5194/os-15-1531-2019>
- Morvan, M., L'Hégaret, P., de Marez, C., Carton, X., Corréard, S., & Baraille, R. (2020). Life cycle of mesoscale eddies in the Gulf of Aden. *Geophysical & Astrophysical Fluid Dynamics*, 1–19. <https://doi.org/10.1080/03091929.2019.1708348>
- Nof, D., Paldor, N., & Gorder, S. V. (2002). The Reddy maker. *Deep Sea Research Part I: Oceanographic Research Papers*, 49(9), 1531–1549. [https://doi.org/10.1016/S0967-0637\(02\)00040-7](https://doi.org/10.1016/S0967-0637(02)00040-7)
- Prasad, T. G., Ikeda, M., & Kumar, S. P. (2001). Seasonal spreading of the Persian Gulf Water mass in the Arabian Sea. *Journal of Geophysical Research*, 106(C8), 17,059–17,071. <https://doi.org/10.1029/2000JC000480>
- Ruddick, B. (1983). A practical indicator of the stability of the water column to double-diffusive activity. *Deep Sea Research Part A. Oceanographic Research Papers*, 30(10), 1105–1107. [https://doi.org/10.1016/0198-0149\(83\)90063-8](https://doi.org/10.1016/0198-0149(83)90063-8)
- Shapiro, G., & Meschanov, S. (1991). Distribution and spreading of Red Sea Water and salt lens formation in the northwest Indian Ocean. *Deep Sea Research Part A. Oceanographic Research Papers*, 38(1), 21–34. [https://doi.org/10.1016/0198-0149\(91\)90052-H](https://doi.org/10.1016/0198-0149(91)90052-H)
- Srinivasan, K., McWilliams, J. C., Molemaker, M. J., & Barkan, R. (2019). Submesoscale vortical wakes in the lee of topography. *Journal of Physical Oceanography*, 49(7), 1949–1971. <https://doi.org/10.1175/JPO-D-18-0042.1>
- Stegner, A., & Dritschel, D. G. (2000). A numerical investigation of the stability of isolated shallow water vortices. *Journal of Physical Oceanography*, 30(10), 2562–2573. [https://doi.org/10.1175/1520-0485\(2000\)030<2562:ANIOTS>2.0.CO;2](https://doi.org/10.1175/1520-0485(2000)030<2562:ANIOTS>2.0.CO;2)
- Turner, J. S. (1979). Buoyancy effects in fluids.
- Vic, C., Rouillet, G., Capet, X., Carton, X., Molemaker, M. J., & Gula, J. (2015). Eddy-topography interactions and the fate of the Persian Gulf Outflow. *Journal of Geophysical Research: Oceans*, 120, 6700–6717. <https://doi.org/10.1002/2015JC011033>
- Zhang, Z., Wang, W., & Qiu, B. (2014). Oceanic mass transport by mesoscale eddies. *Science*, 345(6194), 322–324. <https://doi.org/10.1126/science.1252418>